

Learning Pore-scale Multiphase Flow from 4D Velocimetry

Chunyang Wang,^a Linqi Zhu,^a Yuxuan Gu,^a Robert van der Merwe,^b Xin Ju,^c
Catherine Spurin,^c Samuel Krevor,^a Rex Ying,^d Tobias Pfaff,^e Martin J. Blunt,^a
Tom Bultreys^b and Gege Wen^a

^a Department of Earth Science and Engineering, Imperial College London.

^b Department of Geology, Ghent University.

^c Department of Energy Science and Engineering, Stanford University.

^d Department of Computer Science, Yale University.

^e NVIDIA.

Abstract

Multiphase flow in porous media underpins subsurface energy and environmental technologies, including geological CO₂ storage and underground hydrogen storage, yet pore-scale dynamics in realistic three-dimensional materials remain difficult to characterize and predict. Here we introduce a multimodal learning framework that infers multiphase pore-scale flow directly from time-resolved four-dimensional (4D) micro-velocimetry measurements. The model couples a graph network simulator for Lagrangian tracer-particle motion with a 3D U-Net for voxelized interface evolution. The imaged pore geometry serves as a boundary constraint to the flow velocity and the multiphase interface predictions, which are coupled and updated iteratively at each time step. Trained autoregressively on experimental sequences in capillary-dominated conditions ($Ca \approx 10^{-6}$), the learned surrogate captures transient, nonlocal flow perturbations and abrupt interface rearrangements (Haines jumps) over rollouts spanning seconds of physical time, while reducing hour-to-day-scale direct numerical simulations to seconds of inference. By providing rapid, experimentally informed predictions, the framework opens a route to “digital experiments” to replicate pore-scale physics observed in multiphase flow experiments, offering an efficient tool for exploring injection conditions and pore-geometry effects relevant to subsurface carbon and hydrogen storage.

Introduction

Multiphase transport in porous media is fundamental to a broad class of natural and engineered systems. It is central to the efficiency and security of geological carbon se-

questration^{1–4} and underground hydrogen storage,^{5,6} and plays an important role in related technologies such as fuel-cell water management⁷ and nuclear waste containment.⁸ Across these applications, a substantial portion of transport occurs in capillary-dominated regimes (capillary number $Ca \leq 10^{-6}$), where pore-scale interface dynamics, geometry, and nonlocal flow perturbations exert a first-order control on macroscopic behavior. Accurate prediction of such flows is therefore essential for optimizing system performance while mitigating environmental and societal risks.^{9,10} Fluid flow in porous media is governed by the Navier-Stokes equations,¹¹ and the capillary forces at fluid–fluid interfaces are described by the Young-Laplace equation.¹² Although the underlying equations for multiphase flow through porous media are well established, the practical numerical modeling of multiphase behavior remains a widely recognized challenge due to the complexity of pore-scale interactions and the absence of accurate closure relations across scales.^{13,14}

A key difficulty lies in the spatially and temporally multiscale nature of the multiphase problem, governed by tightly coupled inertial, viscous, capillary, and interfacial forces.^{15–18} Both transient instabilities and persistent sub-pore flow mechanisms — including Haines jumps, wetting layer flow, contact line dynamics, and thin-film breakup — significantly influence larger-scale flow behavior.^{19,20} However, explicitly representing the effect of these sub-pore phenomena in continuum models proves very challenging. Long-range interactions^{21–23} of the flow velocity and multiphase fluid interface prevent a clean decomposition of the dynamics into independent spatial and temporal scales. Multiphase pore-scale flow is commonly investigated using pore-network models, which efficiently explore topology-

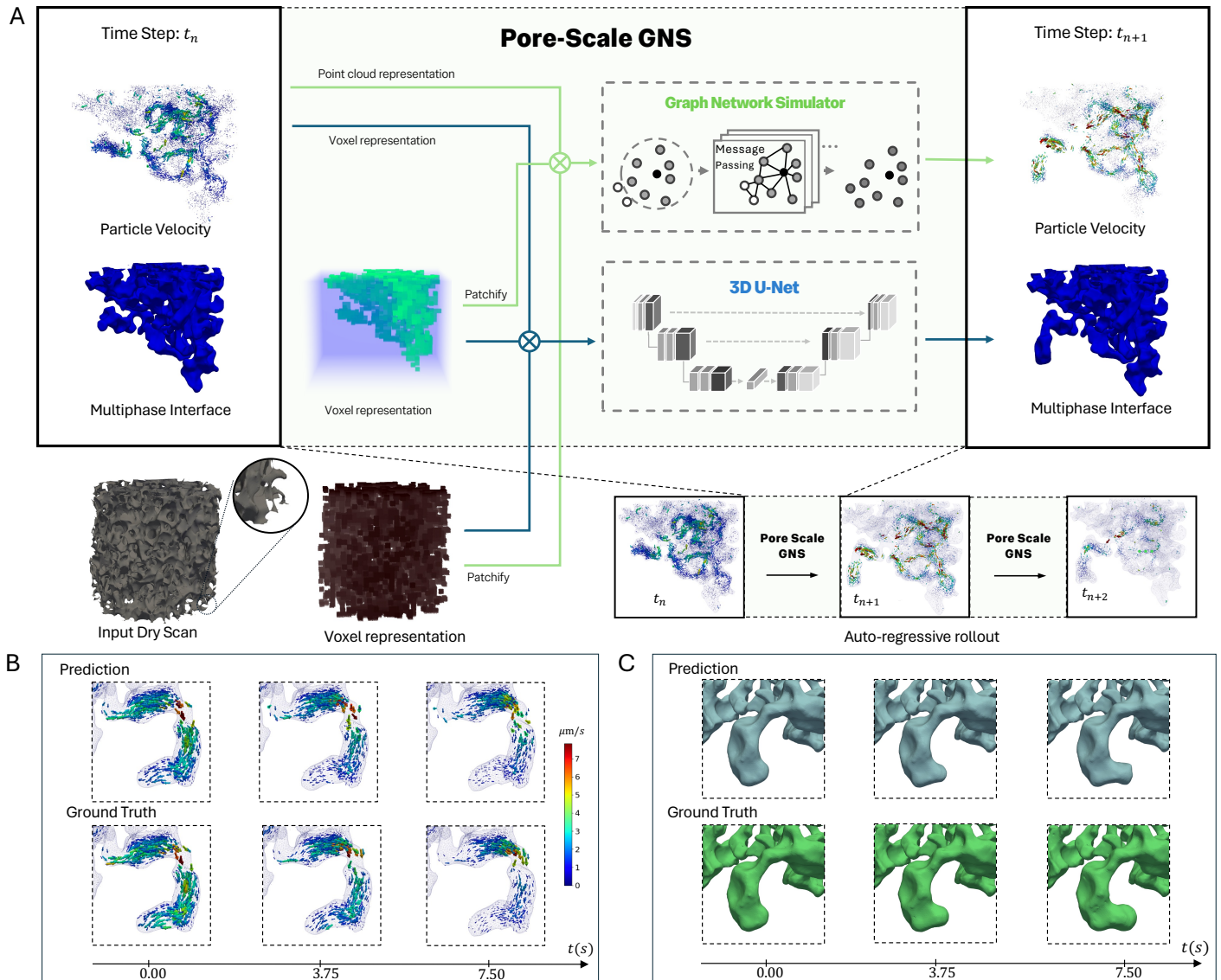


Figure 1 Overview of the Pore Scale GNS framework for learning multiphase fluid dynamics in porous media from 4D velocimetry experimental data. (A) At each time step, the model takes as input the particle velocity field and the multiphase interface, both obtained from high-resolution 4D micro-velocimetry experiments, alongside the static dry image of the pore geometry. These inputs are processed through a multimodal architecture combining a graph neural network and a 3D U-Net. The model is trained to autoregressively predict future states, enabling long-horizon rollout of pore-scale multiphase flow. (B) Representative velocity field predictions over time compared to ground truth, showing the accurate reconstruction of the spatiotemporal flow structures. (C) Corresponding predicted versus actual multiphase interface evolution, demonstrating the model’s ability to recover dynamic interfacial morphology.

controlled displacement but rely on quasi-static invasion rules and idealized throat geometries,²⁴ and mesoscopic lattice Boltzmann methods, which directly resolve interfacial hydrodynamics but are constrained by diffuse-interface assumptions and limited density ratios.²⁵ Both classes of solver face a fundamental nano-to-centimeter scale gap: faithfully representing sub-pore effects requires boundary conditions at nanometer resolution over millimeter-centimeter domains—a constraint that remains computationally intractable. Experimental observations, by con-

trast, intrinsically integrate these sub-pore effects at the observed (micrometer) scale, providing physically consistent data that encode the cumulative influence of fine-scale processes without requiring their explicit resolution.²⁶

Beyond numerical modeling, micro-CT imaging has emerged as a critical approach for understanding multiphase pore-scale phenomena by enabling direct *in situ* observation of flow dynamics in realistic porous materials.²⁷ Modern synchrotron-based facilities now achieve micrometer-scale spatial resolution (μm) and sub-second

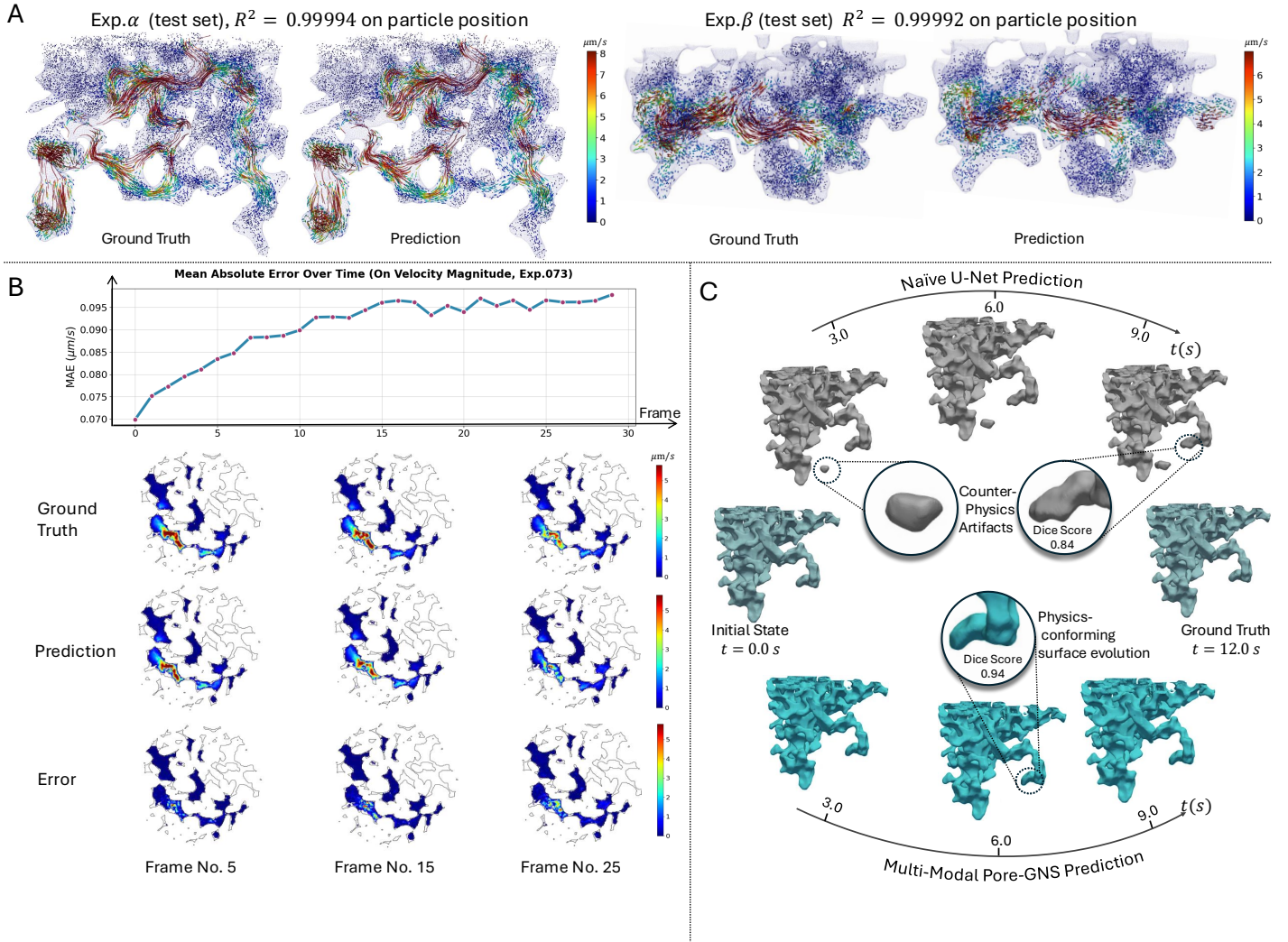


Figure 2 Multimodal prediction of particle-scale flow and fluid interface dynamics. (A) Comparison of predicted and ground truth particle trajectories for two different meniscus configurations. Left: Experiment α , Right: Experiment β . R^2 measured on velocity tracer position prediction for 30 time steps. (B) Temporal evolution of velocity error across 30 frames (top), along with frame-wise comparison of predicted and ground truth flow fields in a representative slice for Exp. α . Error maps highlight that most discrepancies arise near high-gradient regions. (C) Comparison between naïve architecture inference (top path) and multimodal prediction (bottom path) from the same initial interface. The naïve method, relying solely on surface history, introduces nonphysical artifacts (upper center). In contrast, our approach incorporates particle velocity, a complementary modality, to guide interface prediction, effectively avoiding artifacts and producing a physically-consistent geometric surface. Regional Dice Score is reported for the Haines jump area.

temporal resolution (ms),²⁸ leading to key experimental insights such as intermittent gas and liquid transport pathways and previously unresolved mechanisms of phase redistribution.²⁹ When combined with tracer particles, synchrotron-based 4D micro-velocimetry further enables simultaneous, time-resolved measurements of pore-scale velocity fields and fluid–fluid interface evolution, revealing long-range flow responses associated with Haines jumps and other transient interfacial events.³⁰ Additionally, these measurements also offer the spatiotemporal resolution ideal for training machine learning models to directly learn pore-scale multiphase dynamics.

Machine learning (ML) has demonstrated strong capabilities for learning complex phenomena directly from data, with broad successes in natural language processing,³¹ computer vision,³² and computational biology.³³ In fluid mechanics, data-driven surrogates—including convolution-based models such as FluidNet³⁴ and particle-based Graph Network Simulators (GNS)³⁵—have achieved orders-of-magnitude speedups over conventional solvers. However, applying these architectures to porous media poses two key challenges: most existing ML architectures are designed for regular domains or simple geometries,^{36–38} limiting their applicability to irregular pore topologies; and reliable

training data from pore-scale numerical simulations remain scarce because current solvers often simplify or omit critical interfacial and topological complexities.³⁹ High-resolution experimental 4D micro-velocimetry datasets offer a route to overcome both limitations, providing rich, physically consistent observations from which models can learn directly.

Here we introduce the Pore-Scale Graph Network Simulator (Pore-Scale GNS) (Fig. 1), the first ML architecture to directly learn multiphase flow physics from experimental 4D velocimetry data in porous media.³⁰ The framework couples a graph network simulator for Lagrangian tracer-particle dynamics with a 3D U-Net for voxelized interface evolution in a two-way multimodal architecture, using the imaged pore geometry as a boundary constraint and as a shared spatial conditioning input for both velocity and interface predictions. The GNS represents tracer particles as nodes in a dynamically reconstructed graph, with edges connecting neighbors within a physically motivated radius; iterative message passing then propagates local flow information across the network, naturally encoding the long-range velocity correlations that are characteristic of capillary-dominated displacement—a feature that isotropic grid-based methods cannot readily replicate. The 3D U-Net complements this by operating on the voxel grid: its encoder–decoder structure with skip connections is well-suited to capturing the multiscale spatial structure of evolving binary interfaces, and its channel design allows the interpolated GNS velocity field to be ingested directly as a physical conditioning signal, coupling the Lagrangian particle description to the Eulerian interface representation. Trained autoregressively on capillary-dominated drainage sequences, the model generalizes effectively to unseen flow configurations within the same porous medium and, in a zero-shot (no fine-tuning on the target medium) setting, to a substantially different pore structure. These results demonstrate that learning directly from 4D experimental observations can yield physically grounded surrogate models for multiphase transport, opening a path toward rapid “digital experiments” for subsurface energy applications.

Results and Discussion

We design the multimodal ML framework, Pore-Scale GNS (Fig. 1A), to learn multiphase flow dynamics directly from experimental data. Trained on time-resolved 4D micro-velocimetry sequences and evaluated on both temporal extrapolation and structurally distinct test samples, the model recovers particle-scale velocities (Fig. 1B) and fluid–fluid interface evolution (Fig. 1C). The experimental data captures slow, capillary-dominated drainage in a sintered glass porous medium (capillary number $Ca \approx 10^{-6}$,³⁰). It was acquired at the TOMCAT beamline using high-

speed synchrotron micro-CT, providing isotropic voxels of $2.75 \mu\text{m}$ and a field of view of $5.5 \times 5.5 \text{ mm}^2$. Time-resolved 3D tomograms were captured at 0.25 to 0.5 s per frame in bursts of up to 200 scans, simultaneously resolving fluid–fluid interfaces and tracer particle velocities during drainage events.

Two distinct datasets from the same sample are used: Exp. α and β . Exp. β images the lower subvolume of the sintered-glass sample, whereas Exp. α covers the upper subvolume; since the menisci are located in different pore spaces across the two subvolumes, this constitutes a boundary-condition generalization test: the pore geometry is statistically identical between subvolumes, but the meniscus configuration, initial saturation, and mean flow rate differ. In addition, Exp. β features lower mean flow velocities than Exp. α . Exp. α (initial saturation for nonwetting phase $S_{nw}^\alpha = 0.3518$) is used for training: the first 150 frames are provided as input, and the model is rolled forward autoregressively to predict the next 30 frames (~ 7.5 s) as an extrapolation test set. Exp. β , with an initial saturation for the nonwetting phase $S_{nw}^\beta = 0.3576$, occurs prior to Exp. α in physical time. It is originally acquired at a resolution of 0.5 seconds per frame. Through temporal interpolation (refer to Appendix S6), it is resampled to 0.25 seconds per frame and utilized as a test case.

Velocity Prediction Accuracy and Stability over Time

Velocity prediction results reported are evaluated on Exp. α , with the model rolled out autoregressively beyond the training window (Table 1). The trained Pore-Scale GNS shows excellent accuracy for velocity prediction during both training and the extrapolated inference period. As shown in Fig. 2, we evaluate the accuracy of the particle velocity prediction using two methods: streamlines and the interpolated velocity field. The predicted streamline plot in Fig. 2A has highlighted trajectories of particle tracers flowing into the Haines jump region. The streamline tracer particle location prediction achieved an R^2 accuracy of 0.9999 over 30 extrapolation time steps.

Fig. 2B shows that the inference mean absolute error (MAE) of the interpolated velocity field increases gradually over time, but stabilizes below $1.1 \mu\text{m/s}$. Importantly, no significant particle trespassing across the fluid–fluid interface is observed during the autoregressive rollout. This is direct evidence of an effective multimodal design: the interface geometry predicted by the U-Net is explicitly coupled into the GNS velocity prediction at each step, ensuring that particle motion respects the evolving phase boundary (see Fig. 5A). This integration of physical knowledge into the architecture prevents spurious cross-phase transport and

Table 1 Evaluation metrics for fluid topology and velocity prediction across different datasets and rollout settings. Volume and surface area errors are reported as relative percentage errors, while the Dice score quantifies voxel-wise agreement. The velocity field is interpolated based on the predicted tracer velocity. The lower MAE in Exp. β compared to Exp. α is attributed to its lower mean velocity magnitude. The trajectory R^2 measures the coefficient of determination between predicted and ground truth particle positions. All metrics for rollout test sets are averaged over time.

Experiment Setup	Vol. Err. (%)	Surf. Err. (%)	Dice	Vel. MAE ($\mu\text{m/s}$)	Traj. R^2
Exp. α - Train, One-Step (30 Fr.)	0.174	0.220	0.990	0.707	0.9999
Exp. α - Test, One-Step (30 Fr.)	0.187	0.348	0.989	0.738	0.9999
Exp. α - Train, Rollout (30 Fr.)	0.198	0.221	0.985	0.919	0.9999
Exp. α - Test, Rollout (30 Fr.)	0.351	0.613	0.986	1.000	0.9999
Exp. β - Test, One-Step (30 Fr.)	0.683	1.221	0.991	0.098	0.9999
Exp. β - Test, Rollout (30 Fr.)	0.735	1.324	0.990	0.119	0.9999

contributes to the observed stability over long rollout horizons.

Interface Reconstruction and Topological Accuracy

We evaluate the quality of the prediction of the dynamic fluid–fluid interface for Exp. α using three complementary metrics: volume relative error, surface area relative error, and the Dice similarity coefficient⁴⁰ (Table 1). Across both training and test datasets, and for both single-step and long-horizon (30-frame) rollouts, the model demonstrates consistently low volume and surface errors, with Dice scores exceeding 0.98. In the 30-frame rollout, the volume error remains below 0.4 %, and the surface area error is similarly low, thereby demonstrating the model’s capacity to reconstruct physically meaningful interface morphology over time.

A key factor in this performance is the multimodal design of the framework, in which particle velocity predictions from the GNS are incorporated into the U-Net interface reconstruction. Without this conditioning, counter-physical artifacts such as spurious phase emergence in void regions appear, and Dice accuracy deteriorates in regions of rapid interfacial motion. By contrast, including velocity information improves Dice scores in critical regions where Haines jumps occur by 10.6% (Fig. 2C). To achieve this, particle velocities are sampled onto a voxel grid and downsampled to the U-Net input size using the max-pooling scheme shown in Fig. 4B, which preserves over 99% of the information. This approach avoids the severe information loss that typically arises from repeated slicing in three dimensions, ensuring that velocity–interface coupling is maintained at high fidelity.

Generalization across Experiments

Generalization is assessed at three distinct levels: (a) temporal extrapolation beyond the training window within Exp. α ; (b) boundary-condition generalization to a different flow state within the same sintered-glass pore geometry

(Exp. β); and (c) zero-shot cross-rock transfer to a structurally distinct medium (Ketton limestone; *Generalization across Rock Types*). For level (b), we evaluated the trained model on an unseen experiment (Exp. β) that differs from the training case (Exp. α) in meniscus configuration, mean flow rate, and initial saturation, while sharing statistically identical sintered-glass pore geometry. Exp. α features more tortuous pathways with higher average flow velocities, while Exp. β contains a smaller field-of-view and lower average velocities. As shown in Fig. 2A, the model reconstructs velocity streamlines for the unseen experiment with high fidelity, achieving an R^2 score of 0.9992 on Exp. β , measured by predicted particle position—comparable to in-distribution performance—though modest increases in interface volume and surface area errors are observed (Table 1).

The mean MAE of the velocity field is 1.000 $\mu\text{m/s}$ for Exp. α and 0.119 $\mu\text{m/s}$ for Exp. β . These absolute values reflect the substantially different characteristic flow speeds of the two experiments: Exp. β operates at considerably lower velocities, so an order-of-magnitude lower MAE is consistent with comparable relative predictive accuracy. These results suggest that the framework captures generalizable features of multiphase geometry and transport within the same porous medium.

We further validate this generalization under a domain shift by performing strict zero-shot inference on a different rock type: the model trained only on the sintered-glass dataset is applied to an independent drainage experiment in Ketton limestone without fine-tuning. The porous media differ substantially in their void-space structure (mean pore size 122 μm and image-based porosity 27% for the sintered glass filter versus 52 μm and 14% for Ketton). The experiments use the same wetting/nonwetting pair (KI-brine and silicone oil), and both samples are water-wet relative to oil, but the solid surface chemistry differs (glass versus calcite).

With the cross-rock domain shift, predictive performance degrades relative to the in-distribution sintered-glass cases, though the model retains partial predictive capability as detailed below. Fig. 3A shows physically plausible parti-

cle trajectories and velocity structures in the Ketton limestone sample, including within complex pore regions highlighted in the zoomed-in view. At the domain level, predicted and ground-truth velocity statistics show reasonable agreement, though with larger discrepancies than observed for the in-distribution sintered-glass cases. Fig. 3C compares velocity-magnitude distributions; to quantify prediction accuracy we adopt the normalised root-mean-square error relative to the 99th-percentile characteristic velocity (NRMSE_{p99} ; see Appendix S8 for definition and rationale), which is robust to the large fraction of near-stagnant particles present in capillary-dominated drainage. The model achieves $\text{NRMSE}_{p99} = 16.4\%$ on the Ketton dataset, indicating partial but non-trivial statistical agreement with the experimental velocity field under the cross-rock domain shift. Compared to the corresponding in-distribution case (Exp. α), where $\text{NRMSE}_{p99} = 12.5\%$, the error increases to 16.4% for Ketton, consistent with the expected degradation under cross-rock transfer. Alongside this partial agreement, localized degradation occurs in specific pore regions, as highlighted in the failure-mode analysis (Fig. S1, Appendix S2), where reduced trajectory alignment and velocity accuracy reflect the limits of strict zero-shot transfer under substantial pore-structure differences. Fig. 3B further contextualizes this behavior by quantifying domain shifts in pore-scale descriptors between sintered glass and Ketton. Ketton inference uses a model trained on an expanded sintered-glass dataset with two additional sequences (Fig. S2, Appendix S3), improving in-domain robustness while preserving strict zero-shot transfer.

Computational Efficiency

Computational cost for pore-scale numerical simulations depends strongly on domain size, capillary number, initialization scheme, and boundary conditions. For samples of comparable size and flow regime, the effort typically ranges from $O(10^5)$ to $O(10^7)$ time steps, with stringent convergence criteria exerting a major influence on stability and accuracy. Even with substantial computational resources (e.g., 80 parallel NVIDIA V100 GPUs), numerical simulations for cases comparable to ours require between 2 and 20 hours of wall-clock time, depending on capillary number and initialization quality.^{41,42} Critically, this cost grows most severely at low capillary number, where strong interfacial forces demand much tighter convergence and additional iterations per timestep.

In contrast, our framework requires only ~ 200 autoregressive steps to reproduce an experiment of 50 s; inference runs at a constant rate of ~ 0.027 s per step on a single NVIDIA A100 (80 GB), regardless of capillary number or boundary-condition complexity. For comparable capillary-dominated conditions, direct numerical simulations require

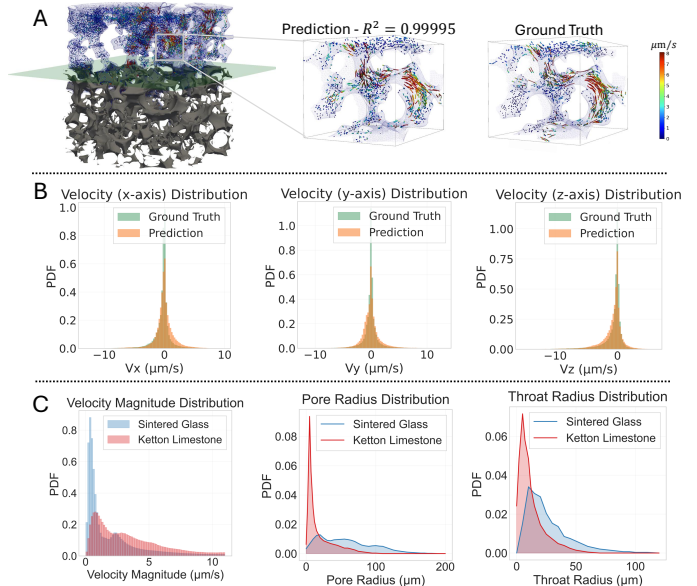


Figure 3 Zero-shot generalization to a new rock type (Ketton). (A) Predicted versus ground-truth particle trajectories and velocity visualization (including a zoomed-in view of the pore space) for an independent drainage experiment in Ketton limestone, evaluated strictly zero-shot (no fine-tuning). The reported R^2 is computed from agreement in particle positions along trajectories. (B) Velocity distribution comparing model predictions with ground truth for Ketton, used to quantify performance under the cross-rock shift. (C) Domain-shift characterization: distributions of key pore-scale descriptors for the training medium (Sintered glass) versus the new medium (Ketton), including pore radius, throat radius, and velocity-magnitude statistics.

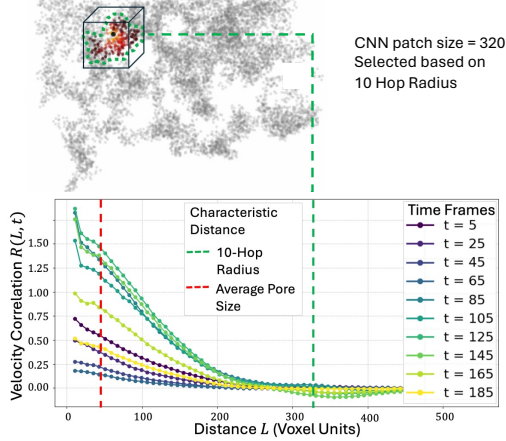
$O(10^4-10^5)$ seconds of wall-clock time, whereas our framework requires ~ 5 seconds, corresponding to a 10^3-10^4 -fold speedup. For training on the same GPU, using the first 150 frames of Experiment α , the wall-clock times were 4 h 8 min for the Graph Network Simulator (GNS) and 48 min for the 3D U-Net. This efficiency gain unlocks pore-scale predictions that were previously computationally intractable.

Physics-Guided Model Architecture Design

We found that the architecture design must reflect the tightly coupled relationship of the fluid-fluid interface geometry and the particle velocity. Ablation studies (see *Materials and Methods*) show that simpler methods, such as a GNS without multimodal information, fail to accurately predict the flow; incorporating particle velocity information enhances the accuracy of interface predictions by 10% measured in Dice Score within the Haines jump region (see Fig. 2C for a zoomed-in view).

We also used the particle flow physics to inform the hyperparameter selection, as shown in Fig. 4A. In the GNS, we chose 10 message passing hops and the local context CNN patch size to be 32 voxels, using the velocity correla-

A Physics-guided hyperparameter selection



B Information-preserving down-sampling technique

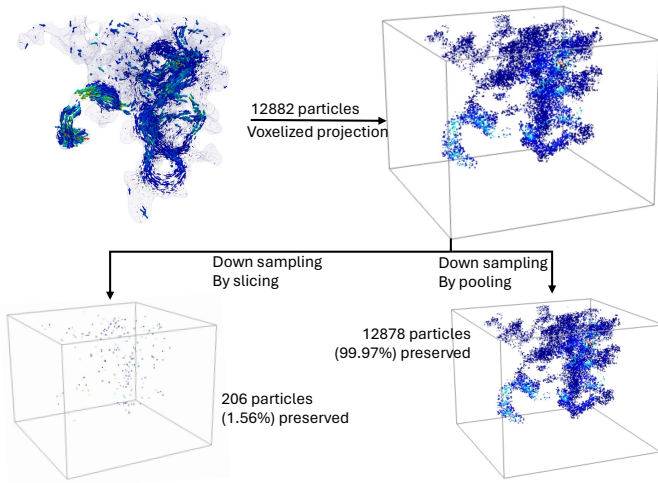


Figure 4 Multimodal information exchange between geometry and velocity. (A) Information from the predicted interface \mathcal{S} is passed from the U-Net surface model to the GNS velocity model by extracting local voxel patches centered on particles. The patch size is selected based on experimental velocity correlation data, shown in the plot. The GNS model uses a 10-hop graph structure, with each hop attending to 32 neighbors, resulting in an effective receptive field of 320 voxels, which corresponds to the spatial extent over which velocity correlations remain significant. (B) Velocity data from particles are transferred to the U-Net by projecting the voxelized velocity onto a 3D grid. Pooling-based downsampling (downsample factor 4 here for demonstration) is applied to reduce memory cost while enabling efficient integration of flow information. Naïve downsampling via slicing leads to severe information loss due to the sparsity and three-dimensional nature of the data (retaining only 1.56% of particles). In contrast, pooling-based downsampling preserves local velocity extremes and retains 99.97% of particles.

tion analysis result, which is ~ 320 voxels. This design allows the Pore-Scale GNS to be informed by the long-range flow dynamics to predict the velocity at the next time step.

Broader Implications

The predictive power demonstrated in this work can be used to advance the understanding of mass transfer processes governed by chemical transport, including fluid–fluid dissolution and mineral dissolution in subsurface environments. Concentration fields in such systems are inherently heterogeneous: values near fluid–fluid and fluid–solid interfaces approach solubility limits, whereas bulk regions remain under-saturated due to incomplete mixing and diffusion constraints.⁴³ In these regimes, both local velocity fields and interfacial geometry are key in controlling transfer efficiency and long-term system evolution.^{43,44} Surface morphology, particularly curvature and topology, governs capillary forces, flow stability, and interphase transfer rates, yet bulk measures such as porosity or permeability fail to capture these transport-relevant features.⁴⁵ By combining particle-resolved velocity with voxel-based interface predictions in a unified framework, our approach provides a physically grounded tool to evaluate phenomena such as capillary trapping, dissolution efficiency, and interfacial stability.

Beyond the specific systems studied here, the velocity–interface coupling framework is applicable to a broader class of subsurface and engineered porous systems where capillary and viscous forces compete, including enhanced oil recovery, reactive transport during mineral dissolution or precipitation, and contaminant migration in remediation systems.

Contribution

This study shows that learning directly from time-resolved, particle-resolved 4D micro-velocimetry provides a distinct route to modeling multiphase flow in porous media. Unlike prior ML efforts that largely relied on static 3D micro-CT to infer scalar properties such as permeability⁴⁶ or on 2D time-series to approximate limited dynamics,⁴⁷ the present approach leverages the full information content of 4D datasets where velocities and interfaces are observed together, yielding more time-resolved and physically grounded predictions. Generalisation experiments demonstrate that the framework transfers effectively to distinct boundary conditions and flow states within the same sintered-glass pore geometry (Exp. β ; boundary-condition generalization), and retains attenuated predictive capability under strict zero-shot transfer to a structurally distinct rock type (Ketton limestone; structural generalization), while highlighting the expected degradation that accompanies pronounced domain shifts.

More broadly, these results position data-driven models trained on rich experimental measurements as a complementary method to first-principles simulation, enabling

rapid exploration of injection scenarios, pore-geometry variations, and flow regimes that remain computationally prohibitive for conventional solvers. The limited diversity of the current training corpus reflects a field-wide constraint: synchrotron-based 4D micro-velocimetry acquisitions demand substantial dedicated beamtime and specialised sample preparation, making comprehensive multi-rock, multi-regime datasets difficult to assemble at this stage of the field’s development. The present work, by demonstrating effective learning from a small number of carefully selected sequences, is intended in part to substantiate the scientific return on such experimental investment. Key next steps are to validate generality beyond the present dataset by expanding to 4D micro-velocimetry acquired across diverse porous materials, wettability states, and flow conditions, to mitigate long-horizon degradation from autoregressive error accumulation (Fig. S1, Appendix S2) through larger, more diverse training data and improved temporal coupling or hybrid physics-informed constraints, and to connect pore-scale predictions to macroscopic descriptors such as relative permeability and capillary pressure curves for direct integration into field-scale subsurface flow models.

Experimental (Materials & Methods)

Dataset and Data Processing

The dataset used in this work was obtained through the 4D micro-velocimetry experimental procedure of Bultreys et al.,³⁰ which provides direct, time-resolved measurements of pore-scale flow and interface dynamics. This dataset captures complex pore-scale phenomena, including Haines jumps, long-range velocity perturbations, and highly tortuous flow paths, providing a rich experimental foundation for data-driven modeling of multiphase flow.

This experiment tracked the displacement of viscous silicone oil into brine-saturated sintered glass filters (mean pore size 122 μm , porosity 27%) using tracer particles (10 μm diameter, silver-coated hollow spheres) at a controlled injection rate corresponding to a capillary number of approximately 5.5×10^{-6} . The imaging was performed at the TOMCAT beamline (Swiss Light Source) with 2.75 μm voxel resolution and 0.25 s temporal resolution, enabling full 3D reconstruction of both the multiphase fluid interface and Lagrangian particle trajectories over a 50-second time window. Particles were detected on each tomogram in the time series using local grey value peak detection. These detections were subsequently linked into particle trajectories using a location-prediction-based nearest-neighbour algorithm, implemented using the open-source TrackPy pack-

age.⁴⁸ We applied a constant-acceleration Kalman filter with Rauch–Tung–Striebel (RTS) smoothing to the particle trajectories to mitigate localization noise and obtain physically plausible velocity estimates for subsequent model training (see Appendix S7).

Model Design

Our framework integrates two coupled components: a Graph Network-based Simulator (GNS) for particle velocity prediction, and a 3D U-Net for reconstructing multiphase fluid interfaces. Both components are informed by pore geometry and exchange information at each time step, enabling multimodal learning from experimental data.

Graph Network-based Simulator (GNS): The GNS models particle dynamics represented in a Lagrangian framework.³⁵ Each particle at time step t is described by a feature vector

$$\mathbf{x}_i^{(t)} = \left[\mathbf{p}_i^{(t-1)}, \mathbf{p}_i^{(t)}, \dot{\mathbf{p}}_i^{(t-1)}, \dots, \dot{\mathbf{p}}_i^{(t-C)} \right] \in \mathbb{R}^{3C+6},$$

which contains the particle’s positions at time steps $t-1$ and t , along with historical velocity information from the past C steps $\{\dot{\mathbf{p}}_i^{(\tau)}\}_{\tau=t-C}^{t-1}$. Pairwise particle interactions are encoded using a dynamically constructed graph, where edges are defined via a radius-based connectivity criterion:

$$\mathcal{E}^{(t)} = \left\{ (i, j) \mid \|\mathbf{p}_i^{(t)} - \mathbf{p}_j^{(t)}\|_2 < r \right\},$$

with $\mathbf{p}_i^{(t)} \in \mathbb{R}^3$ denoting the position of particle i , and $r = 32$ voxels representing the interaction radius, selected based on physical flow correlation length (see Fig. 4A). For each edge, the raw features $\mathbf{d}_{ij}^{(t)}$ include historical relative positional displacements and their combined magnitude. Specifically,

$$\mathbf{d}_{ij}^{(t)} = \left[\delta_{ij}^{(t)}, \|\delta_{ij}^{(t)}\|_2 \right] \in \mathbb{R}^7,$$

where the historical relative displacement is

$$\delta_{ij}^{(t)} = [(\mathbf{p}_i^{(t)} - \mathbf{p}_j^{(t)}), (\mathbf{p}_i^{(t-1)} - \mathbf{p}_j^{(t-1)})] \in \mathbb{R}^6.$$

Notably, both raw node and edge features are normalized to have zero mean and unit variance. After extracting raw features, the node and edge feature embeddings are obtained via encoders ϕ_{node} and ϕ_{edge} , respectively, *i.e.*

$$\mathbf{h}_i^{(t)} = \phi_{\text{node}}(\mathbf{x}_i^{(t)}), \quad \mathbf{e}_{ij}^{(t)} = \phi_{\text{edge}}(\mathbf{d}_{ij}^{(t)}).$$

Pore geometry information is incorporated via a convolutional neural network-based image encoder $\phi_{\text{image}}(\mathcal{G}, \hat{\mathcal{S}}^{(t)})$, which processes localized voxel patches extracted from the full CT scan of the dry pore space \mathcal{G} , and current mul-

tiphase interface $\hat{\mathcal{S}}^{(t)}$ predicted by U-Net (see *3D U-Net for Interface Prediction*). These patches, centered on each particle, capture the nearby pore geometric environment relevant to local flow behavior. The encoded geometry features are then added to particle representations, enabling pore geometry-conditioned dynamics:

$$\mathbf{h}_i^{(t,0)} \leftarrow \mathbf{h}_i^{(t)} + \phi_{\text{image}}(\mathcal{G}, \hat{\mathcal{S}}^{(t)}),$$

where $\mathbf{h}_i^{(t,0)}$ denotes the initial node representation before message passing. The GNS backbone consists of a stack of $L = 10$ message-passing layers. Within each layer $l \in [0, 9]$ at time t , edges features are first updated as

$$\mathbf{e}_{ij}^{(t,l)} \leftarrow \mathbf{e}_{ij}^{(t,l)} + \phi_{\text{edge-update}}(\mathbf{h}_i^{(t,l)}, \mathbf{h}_j^{(t,l)}, \mathbf{e}_{ij}^{(t,l)}),$$

followed by the node update

$$\mathbf{h}_i^{(t,l)} \leftarrow \mathbf{h}_i^{(t,l)} + \phi_{\text{node-update}}\left(\mathbf{h}_i^{(t,l)}, \sum_{j \in \mathcal{N}(i)} \mathbf{e}_{ij}^{(t,l)}\right),$$

where $\mathcal{N}(i)$ denotes the neighbors of node i . The outputs $\mathbf{e}_{ij}^{(t,l)}$ and $\mathbf{h}_i^{(t,l)}$ serve as the input to the next layer $l + 1$. After L iterations, the final node embeddings $\mathbf{h}_i^{(t,L)}$ are decoded to predict the current particle velocities:

$$\hat{\mathbf{v}}_i^{(t)} = \phi_{\text{decode}}(\mathbf{h}_i^{(t,L)}).$$

Note that $\phi_{\text{node}}, \phi_{\text{edge}}, \phi_{\text{edge-update}}, \phi_{\text{node-update}}$ are all multi-layer perceptrons (MLPs). The model is trained using a normalized mean squared error (MSE) loss between predicted and ground truth particle velocities based on one-step prediction, while Gaussian noise is added to particle positions to improve rollout robustness (see Appendix S1 for details). During inference, multi-step trajectories are generated autoregressively by updating particle positions using a central-difference update. At each step, the graph is reconstructed based on the updated positions, ensuring that message passing reflects the evolving flow topology. This dynamic recomputation helps maintain physical plausibility and prevents error accumulation in long rollouts.

3D U-Net for Interface Prediction: The multiphase interface is modeled as a voxel occupancy field $\mathcal{S}^{(t)}$, representing the non-wetting fluid phase at time t . The U-Net takes as input a sequence of N_{in} previous occupancy fields, along with the downsampled voxelized velocity field interpolated from the GNS outputs. Input channels per voxel include:

$$\mathcal{I} = \left\{ \mathcal{S}^{(t-N_{\text{in}}+1)}, \dots, \mathcal{S}^{(t)}, \mathcal{V}_x^{(t)}, \mathcal{V}_y^{(t)}, \mathcal{V}_z^{(t)}, \mathcal{G} \right\},$$

where $\mathcal{V}_x^{(t)}, \mathcal{V}_y^{(t)}, \mathcal{V}_z^{(t)}$ denote the velocity components along the three orthogonal spatial directions and \mathcal{G} is the static pore geometry mask, the model is trained using a voxel-wise binary cross-entropy loss.

The network architecture follows an encoder-decoder design with skip connections. Each downsampling stage consists of a 3D max-pooling layer followed by two 3D convolutions with batch normalization and ReLU activations. The number of feature channels doubles at each level of the encoder. The decoder mirrors this pattern using transposed convolutions for upsampling and concatenating the corresponding encoder features to retain spatial information. Formally, the prediction for the next interface frame is given by:

$$\hat{\mathcal{S}}^{(t+1)} = \text{U-Net}(\mathcal{I}).$$

To integrate particle-derived velocity information into the grid-based U-Net while reducing memory cost, we apply an information-preserving pooling operation (Fig. 4B, see Appendix S4 for a detailed description). This downsampling strategy, in contrast to naïve slicing or averaging, selectively retains local velocity extremes within each pooling block, thereby preserving more than 99% of the particle information despite an eight-fold reduction in resolution.

Multimodal Inference: Coupled Velocity and Interface Prediction

The proposed framework combines particle-based velocity modeling with voxelized interface prediction in a tightly coupled, multimodal setting. This allows for coherent long-horizon rollouts of multiphase flow that respect both fluid dynamics and evolving surface morphology.

At each time step t , the system predicts:

1. Particle velocities $\hat{\mathbf{v}}_i^{(t)}$ using the Graph Network-based Simulator (GNS).
2. The updated multiphase interface $\hat{\mathcal{S}}^{(t+1)}$ using a 3D U-Net conditioned on velocity fields and pore geometry.

Algorithm 1 outlines the workflow. The coupled architecture respects both Lagrangian particle motion and Eulerian voxel-based interface representations.

Model Ablation and Variants

To assess the robustness of our architecture, we performed the following ablation experiments.

We first examined the performance of the GNS model when it is stripped of information about the multiphase interface and the solid pore structure. In the full multimodal formulation, the model takes as input particle states together with pore geometry and interface information, which we write as $\text{GNS}(\{\mathbf{p}_i^{(t)}\}, \{\mathcal{S}^{(t)}\}, \mathcal{G})$; in the ablated

Algorithm 1 Multimodal Rollout of Velocity and Interface Evolution

- 1: **Input:** Initial particle position history $\{\mathbf{p}_i^{(t)}\}_{t=\tau-1}^\tau$, velocity history $\{\dot{\mathbf{p}}_i^{(t)}\}_{t=\tau-C}^{\tau-1}$, interface history $\{\mathcal{S}^{(t)}\}_{t=\tau-N_{\text{in}}+1}^\tau$, pore geometry \mathcal{G} , and graph radius r
- 2: **for** each time step $t = \tau, \tau + 1, \tau + 2, \dots$ **do**
- 3: **Predict particle velocities** using GNS:

$$\hat{\mathbf{v}}_i^{(t)} \leftarrow \text{GNS} \left(\{\mathbf{p}_i^{(t)}\}, \{\dot{\mathbf{p}}_i^{(t)}\}, \{\mathcal{S}^{(t)}\}, \mathcal{G} \right)$$

- 4: **Update particle positions:**

$$\mathbf{p}_i^{(t+1)} \leftarrow \mathbf{p}_i^{(t)} + 2\hat{\mathbf{v}}_i^{(t)}$$

- 5: **Recompute graph structure:**

$$\mathcal{E}^{(t+1)} \leftarrow \left\{ (i, j) \mid \|\mathbf{p}_i^{(t+1)} - \mathbf{p}_j^{(t+1)}\|_2 < r \right\}$$

- 6: **Interpolate velocities to voxel grid:**

$$\mathcal{V}^{(t)} \leftarrow \text{Interpolate} \left(\mathbf{p}_i^{(t+1)}, \hat{\mathbf{v}}_i^{(t)} \right)$$

- 7: **Prepare multimodal input for U-Net:**

$$\mathcal{I} \leftarrow \left\{ \mathcal{S}^{(t-N_{\text{in}}+1)}, \dots, \mathcal{S}^{(t)}, \mathcal{V}_x^{(t)}, \mathcal{V}_y^{(t)}, \mathcal{V}_z^{(t)}, \mathcal{G} \right\}$$

- 8: **Predict next interface using U-Net:**

$$\hat{\mathcal{S}}^{(t+1)} \leftarrow \text{U-Net}(\mathcal{I})$$

- 9: **Update interface history with $\hat{\mathcal{S}}^{(t+1)}$**

- 10: **Condition next GNS input on $\hat{\mathcal{S}}^{(t+1)}$**

- 11: **end for**
-

setting, the model is reduced to $\text{GNS}(\{\mathbf{p}_i^{(t)}\})$, receiving no explicit geometric conditioning. This simplification produced strongly unphysical behavior: particle trajectories were predicted to escape from the nonwetting phase region, a violation of the governing physics (Fig. 5A). This experiment demonstrates that coupling GNS to both solid structure and dynamic interface geometry is indispensable for consistent rollout predictions.

Multiphase interface geometry plays a critical role in predicting the evolution of particle trajectories. In Fig. 5B, we investigated how best to represent this information. To this end, we benchmarked the U-Net model architecture⁴⁹ against several of the most recent advanced approaches.

We evaluated two classes of learned 3D representations: triplane-based encoder-decoder and VecSet-based surface representations. In triplane models, a 3D point $\mathbf{x} \in \mathbb{R}^3$ is projected onto three orthogonal 2D planes (xy, xz, yz), and its occupancy is predicted as $\hat{\mathbf{O}} = NN_\phi(\mathbf{x}, \mathbf{f}_{xy}, \mathbf{f}_{xz}, \mathbf{f}_{yz})$,

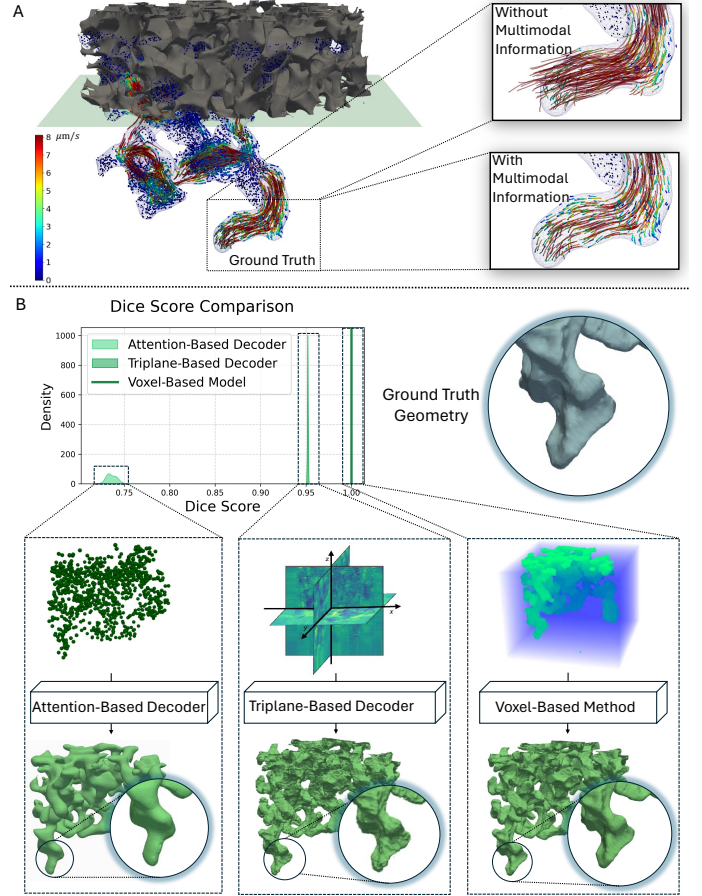


Figure 5 Ablation Experiments. (A) The sintered glass matrix (gray) under the green plane is made transparent to expose the non-wetting phase (blue). Velocity tracer trajectories are color-mapped by their instantaneous velocity magnitude. When interface and pore structure inputs are removed from the GNS, particles exhibit unphysical behavior, including escaping beyond the fluid interface in the Haines jump region. (B) Geometry representation benchmarks: triplane and VecSet degrade interface detail, while voxel-based U-Net reconstructions preserve ground truth geometry.

where $\{\mathbf{f}_{xy}, \mathbf{f}_{xz}, \mathbf{f}_{yz}\}$ are learned feature maps encoding geometry from each plane.^{50,51} VecSet models, in contrast, encode the geometry as a set of latent vectors $\{\mathbf{z}_1, \dots, \mathbf{z}_N\}$ derived from sampled surface points.⁵² The occupancy of a query point is decoded via attention-based aggregation over these latent codes. Both models were trained on 150 samples and tested on 50 unseen geometries. Qualitatively, triplane reconstructions were noisy and lacked local consistency, while VecSet results were overly smoothed and failed to resolve detailed curvature. Quantitatively, Dice similarity scores averaged 0.952 for triplane and 0.736 for VecSet, while the U-Net model consistently achieved scores approaching unity.

To investigate how the velocity information from GNS model affects multiphase interface prediction, the full

model—which incorporates interface history, velocity field, and pore geometry:

$$\text{U-Net} \left(\left\{ \mathcal{S}^{(t-N_{\text{in}}+1)}, \dots, \mathcal{S}^{(t)}, \mathcal{V}_x^{(t)}, \mathcal{V}_y^{(t)}, \mathcal{V}_z^{(t)}, \mathcal{G} \right\} \right),$$

is compared against a naïve variant that omits the velocity field:

$$\text{U-Net} \left(\left\{ \mathcal{S}^{(t-N_{\text{in}}+1)}, \dots, \mathcal{S}^{(t)}, \mathcal{G} \right\} \right).$$

The naïve model generated non-physical artifacts such as disconnected fluid regions and inconsistent boundary evolution. Including the velocity field improved the Dice score from 0.84 to 0.94 and eliminated these pathologies, highlighting the importance of velocity in interface prediction, as shown in Fig. 2C.

These ablations highlight the interdependence between accurate geometric conditioning and reliable interface representation. The performance of GNS degrades significantly without explicit access to interface and structure information, and our benchmarks show that among candidate representations, voxel-based U-Nets best preserve the geometric fidelity required for physically plausible predictions. This tight coupling between accurate geometry and consistent rollout dynamics is especially critical in porous media, where small-scale interface features directly influence capillary phenomena and phase behavior.⁴⁵

Author Contributions

C.W., L.Z., Y.G., and G.W. designed research; C.W., Y.G., L.Z., and G.W. performed research; R.v.d.M. and T.B. contributed data and interpretation; C.W., Y.G., L.Z., X.J., C.S., and R.Y. contributed to code development; C.W. and Y.G. analyzed data; G.W., T.P., S.K., and M.J.B. supervised the research; G.W. project administration, funding acquisition; C.W. wrote the original draft. All authors reviewed and edited the draft.

Conflicts of Interest

The authors declare no competing interest.

Data Availability

Source code for the proposed model, training and benchmarking code are available at GitHub (https://github.com/chunyang-w/pore_gns). The pore-scale experimental datasets used in this study are publicly available in the PSI Public Data Repository (<https://doi.org/10.16907/c0dfa6c8-25da-454e-82fa-fc5db7f7c6f2>).

Acknowledgements

C.W. acknowledges the support of the Department of Earth Science and Engineering, Imperial College London, through

a Janet Watson PhD Fellowship. L.Z. and G.W. acknowledge the generous support of Schmidt Sciences through the AI2050 fellowship. T.B. and R.v.d.M. are supported by an ERC grant (FLOWSCOPY, 101116228) funded by the European Union. Views and opinions expressed are, however, those of the author(s) only and do not necessarily reflect those of the European Union or the European Research Council Executive Agency. Neither the European Union nor the granting authority can be held responsible for them. The experimental data reused in this work were acquired at the TOMCAT beamline X02DA of the SLS, Paul Scherrer Institut, Villigen, Switzerland (beam time proposal 20212066).

Notes and References

- [1] Rebecca L. Siegelman, Eugene J. Kim, and Jeffrey R. Long. Porous materials for carbon dioxide separations. *Nature Materials*, 20(8):1060–1072, August 2021. ISSN 1476-4660. doi: 10.1038/s41563-021-01054-8. URL <https://doi.org/10.1038/s41563-021-01054-8>.
- [2] Jialei Chen, Tiantian Lu, Xuelong Liao, Shan Chen, Youzeng Li, Yue Wang, Runyu Lv, Wenyue Cui, Wenlong Lan, Wei Wang, Lixin Cao, Zhuo Chen, Zhuang Zhao, Jinhan Li, Wei Shi, Sheng Zhang, and Huan Wang. Nutrient diffusion-inspired catalysts with self-reinforced concentration gradient for sustainable electroreduction of dilute CO_2 . *Nature Communications*, 16(1):7598, August 2025. ISSN 2041-1723. doi: 10.1038/s41467-025-62240-9. URL <https://doi.org/10.1038/s41467-025-62240-9>.
- [3] Gayea Hyun, Jun Tae Song, Changui Ahn, Youngjin Ham, Donghwi Cho, Jihun Oh, and Seokwoo Jeon. Hierarchically porous au nanostructures with interconnected channels for efficient mass transport in electrocatalytic CO_2 reduction. *Proceedings of the National Academy of Sciences*, 117(11):5680–5685, 2020. doi: 10.1073/pnas.1918837117. URL <https://www.pnas.org/doi/abs/10.1073/pnas.1918837117>.
- [4] R. K. Pachauri, M. R. Allen, V. R. Barros, J. Broome, W. Cramer, R. Christ, J. A. Church, L. Clarke, Q. Dahe, P. Dasgupta, N. K. Dubash, O. Edenhofer, I. Elgizouli, C. B. Field, P. Forster, P. Friedlingstein, J. Fuglestedt, L. Gomez-Echeverri, S. Hallegatte, G. Hegerl, M. Howden, K. Jiang, B. Jimenez Cisneroz, V. Kattsov, H. Lee, K. J. Mach, J. Marotzke, M. D. Mastrandrea, L. Meyer, J. Minx, Y. Mulugetta, K. O’Brien, M. Oppenheimer, J. J. Pereira, R. Pichs-Madruga, G.-K. Plattner, Hans-Otto Pörtner, S. B. Power, B. Preston, N. H. Ravindranath, A. Reisinger, K. Riahi, M. Rusticucci, R. Scholes, K. Seyboth,

- Y. Sokona, R. Stavins, T. F. Stocker, P. Tschakert, D. van Vuuren, and J.-P. van Ypersele. Climate Change 2014: Synthesis Report. Contribution of Working Groups I, II and III to the Fifth Assessment Report of the Intergovernmental Panel on Climate Change. IPCC, Geneva, Switzerland, 2014.
- [5] Hyunchul Oh, Nikolay Tumanov, Voraksmay Ban, Xiao Li, Bo Richter, Matthew R. Hudson, Craig M. Brown, Gail N. Iles, Dirk Wallacher, Scott W. Jorgensen, Luke Daemen, Rafael Balderas-Xicohtencatl, Yongqiang Cheng, Anibal J. Ramirez-Cuesta, Michael Heere, Sergio Posada-Pérez, Geoffroy Hautier, Michael Hirscher, Torben R. Jensen, and Yaroslav Filinchuk. Small-pore hydridic frameworks store densely packed hydrogen. Nature Chemistry, 16(5):809–816, May 2024. ISSN 1755-4349. doi: 10.1038/s41557-024-01443-x. URL <https://doi.org/10.1038/s41557-024-01443-x>.
- [6] Hyesun Kim, Hyeonji Kim, Wonsik Kim, Choah Kwon, Si-Won Jin, Taejun Ha, Jae-Hyeok Shim, Soohyung Park, Aqil Jamal, Sangtae Kim, and Eun Seon Cho. Facile synthesis of nanoporous mg crystalline structure by organic solvent-based reduction for solid-state hydrogen storage. Nature Communications, 15(1):10800, December 2024. ISSN 2041-1723. doi: 10.1038/s41467-024-55018-y. URL <https://doi.org/10.1038/s41467-024-55018-y>.
- [7] Mengnan Wang, Jianguang Zhang, Silvia Favero, Luke J. R. Higgins, Hui Luo, Ifan E. L. Stephens, and Maria-Magdalena Titirici. Resolving optimal ionomer interaction in fuel cell electrodes via operando x-ray absorption spectroscopy. Nature Communications, 15(1):9390, October 2024. ISSN 2041-1723. doi: 10.1038/s41467-024-53823-z. URL <https://doi.org/10.1038/s41467-024-53823-z>.
- [8] Baiyan Li, Xinglong Dong, Hao Wang, Dingxuan Ma, Kui Tan, Stephanie Jensen, Benjamin J. Deibert, Joseph Butler, Jeremy Cure, Zhan Shi, Timo Thonhauser, Yves J. Chabal, Yu Han, and Jing Li. Capture of organic iodides from nuclear waste by metal-organic framework-based molecular traps. Nature Communications, 8(1):485, September 2017. ISSN 2041-1723. doi: 10.1038/s41467-017-00526-3. URL <https://doi.org/10.1038/s41467-017-00526-3>.
- [9] Julien Mouli-Castillo, Mark Wilkinson, Dimitri Mignard, Christopher McDermott, R. Stuart Haszeldine, and Zoe K. Shipton. Inter-seasonal compressed-air energy storage using saline aquifers. Nature Energy, 4(2):131–139, February 2019. ISSN 2058-7546. doi: 10.1038/s41560-018-0311-0. URL <https://doi.org/10.1038/s41560-018-0311-0>.
- [10] Mai Bui, Claire S. Adjiman, André Bardow, Edward J. Anthony, Andy Boston, Solomon Brown, Paul S. Fennell, Sabine Fuss, Amparo Galindo, Leigh A. Hackett, Jason P. Hallett, Howard J. Herzog, George Jackson, Jasmin Kemper, Samuel Krevor, Geoffrey C. Maitland, Michael Matuszewski, Ian S. Metcalfe, Camille Petit, Graeme Puxty, Jeffrey Reimer, David M. Reiner, Edward S. Rubin, Stuart A. Scott, Nilay Shah, Berend Smit, J. P. Martin Trusler, Paul Webley, Jennifer Wilcox, and Niall Mac Dowell. Carbon capture and storage (CCS): the way forward. Energy Environ. Sci., 11:1062–1176, 2018. doi: 10.1039/C7EE02342A. URL <http://dx.doi.org/10.1039/C7EE02342A>.
- [11] Grétar Tryggvason, Ruben Scardovelli, and Stéphane Zaleski. Direct numerical simulations of gas–liquid multiphase flows. Cambridge university press, 2011.
- [12] L W Lake. Enhanced oil recovery. Old Tappan, NJ; Prentice Hall Inc., 12 1988. URL <https://www.osti.gov/biblio/5112525>.
- [13] Ryan T. Armstrong, James E. McClure, Mark A. Berrill, Maja Rücker, Steffen Schlüter, and Steffen Berg. Beyond darcy’s law: The role of phase topology and ganglion dynamics for two-fluid flow. Physical Review E, 94(4):043113, October 2016. ISSN 2470-0045, 2470-0053. doi: 10.1103/PhysRevE.94.043113. URL <https://link.aps.org/doi/10.1103/PhysRevE.94.043113>.
- [14] Yihuai Zhang, Branko Bijeljic, Ying Gao, Qingyang Lin, and Martin J. Blunt. Quantification of nonlinear multiphase flow in porous media. Geophysical Research Letters, 48(5):e2020GL090477, 2021. doi: <https://doi.org/10.1029/2020GL090477>. URL <https://agupubs.onlinelibrary.wiley.com/doi/abs/10.1029/2020GL090477>. e2020GL090477 2020GL090477.
- [15] Kamaljit Singh, Michael Jung, Martin Brinkmann, and Ralf Seemann. Capillary-dominated fluid displacement in porous media, 2019. ISSN 1545-4479. URL <https://www.annualreviews.org/content/journals/10.1146/annurev-fluid-010518-040342>.
- [16] Sujit S. Datta, H. Chiang, T. S. Ramakrishnan, and David A. Weitz. Spatial fluctuations of fluid velocities in flow through a three-dimensional porous medium. Phys. Rev. Lett., 111:064501, Aug 2013. doi: 10.1103/PhysRevLett.111.064501. URL <https://link.aps.org/doi/10.1103/PhysRevLett.111.064501>.
- [17] Sujit S Datta, Jean-Baptiste Dupin, and David A Weitz. Fluid breakup during simultaneous two-phase flow through a three-dimensional porous medium. Physics of Fluids, 26(6):062004, 2014.
- [18] Francisco J Carrillo, Ian C Bourg, and Cyprien

- Soulaine. Multiphase flow modeling in multiscale porous media: An open-source micro-continuum approach. *Journal of Computational Physics*: X, 8: 100073, 2020.
- [19] Andrea Ferrari, Joaquin Jimenez-Martinez, Tanguy Le Borgne, Yves Méheust, and Ivan Lunati. Challenges in modeling unstable two-phase flow experiments in porous micromodels. *Water Resources Research*, 51(3):1381–1400, 2015. doi: <https://doi.org/10.1002/2014WR016384>. URL <https://agupubs.onlinelibrary.wiley.com/doi/abs/10.1002/2014WR016384>.
- [20] Benzhong Zhao, Christopher W. MacMinn, Bauyrzhan K. Primkulov, Yu Chen, Albert J. Valocchi, Jianlin Zhao, Qinjun Kang, Kelsey Bruning, James E. McClure, Cass T. Miller, Abbas Fakhari, Diogo Bolster, Thomas Hiller, Martin Brinkmann, Luis Cueto-Felgueroso, Daniel A. Cogswell, Rahul Verma, Maša Prodanović, Julien Maes, Sebastian Geiger, Morten Vassvik, Alex Hansen, Enrico Segre, Ran Holtzman, Zhibing Yang, Chao Yuan, Bruno Chareyre, and Ruben Juanes. Comprehensive comparison of pore-scale models for multiphase flow in porous media. *Proceedings of the National Academy of Sciences*, 116(28):13799–13806, 2019. doi: [10.1073/pnas.1901619116](https://doi.org/10.1073/pnas.1901619116). URL <https://www.pnas.org/doi/abs/10.1073/pnas.1901619116>.
- [21] Steffen Berg, Holger Ott, Stephan A. Klapp, Alex Schwing, Rob Neiteler, Niels Brussee, Axel Makurat, Leon Leu, Frieder Enzmann, Jens-Oliver Schwarz, Michael Kersten, Sarah Irvine, and Marco Stambanoni. Real-time 3d imaging of haines jumps in porous media flow. *Proceedings of the National Academy of Sciences*, 110(10):3755–3759, 2013. doi: [10.1073/pnas.1221373110](https://doi.org/10.1073/pnas.1221373110). URL <https://www.pnas.org/doi/abs/10.1073/pnas.1221373110>.
- [22] Ryan T. Armstrong and Steffen Berg. Interfacial velocities and capillary pressure gradients during haines jumps. *Phys. Rev. E*, 88:043010, Oct 2013. doi: [10.1103/PhysRevE.88.043010](https://doi.org/10.1103/PhysRevE.88.043010). URL <https://link.aps.org/doi/10.1103/PhysRevE.88.043010>.
- [23] Mahdi Mansouri-Boroujeni, Cyprien Soulaine, Mohamed Azaroual, and Sophie Roman. How interfacial dynamics controls drainage pore-invasion patterns in porous media. *Advances in Water Resources*, 171: 104353, 2023.
- [24] Martin J. Blunt. Flow in porous media — pore-network models and multiphase flow. *Current Opinion in Colloid & Interface Science*, 6(3):197–207, 2001. ISSN 1359-0294. doi: [https://doi.org/10.1016/S1359-0294\(01\)00084-X](https://doi.org/10.1016/S1359-0294(01)00084-X). URL <https://www.sciencedirect.com/science/article/pii/S135902940100084X>.
- [25] C. Pan, M. Hilpert, and C. T. Miller. Estimating permeability of 3d micro-ct images by physics-informed cnns based on dns. *Computational Geosciences*, 27(2):245–262, April 2023. ISSN 1573-1499. doi: [10.1007/s10596-022-10184-0](https://doi.org/10.1007/s10596-022-10184-0). URL <https://doi.org/10.1007/s10596-022-10184-0>.
- [26] Shan Wang, Catherine Spurin, and Tom Bultreys. Pore-scale imaging of multiphase flow fluctuations in continuum-scale samples. *Water Resources Research*, 59(6):e2023WR034720, 2023. doi: <https://doi.org/10.1029/2023WR034720>. URL <https://agupubs.onlinelibrary.wiley.com/doi/abs/10.1029/2023WR034720>. e2023WR034720
- [27] Dorte Wildenschild and Adrian P. Sheppard. X-ray imaging and analysis techniques for quantifying pore-scale structure and processes in subsurface porous medium systems. *Advances in Water Resources*, 51:217–246, 2013. ISSN 0309-1708. doi: <https://doi.org/10.1016/j.advwatres.2012.07.018>. URL <https://www.sciencedirect.com/science/article/pii/S0309170812002060>.
- [28] Ivan Gorenkov, Viktor Nikitin, Mikhail Fokin, and Anton Duchkov. Projection–subtraction x-ray imaging scheme for studying fast fluid-dynamics processes in porous media. *Transport in Porous Media*, 151(3): 625–643, February 2024. ISSN 1573-1634. doi: [10.1007/s11242-023-02055-8](https://doi.org/10.1007/s11242-023-02055-8). URL <https://doi.org/10.1007/s11242-023-02055-8>.
- [29] Catherine Spurin, Tom Bultreys, Branko Bijeljic, Martin J Blunt, and Samuel Krevor. Intermittent fluid connectivity during two-phase flow in a heterogeneous carbonate rock. *Physical Review E*, 100(4):043103, 2019.
- [30] Tom Bultreys, Sharon Ellman, Christian M. Schlepütz, Matthieu N. Boone, Gülce Kalyoncu Pakkaner, Shan Wang, Mostafa Borji, Stefanie Van Offenwert, Niloofar Moazami Goudarzi, Wannes Goethals, Chandra Widyananda Winardhi, and Veerle Cnudde. 4d microvelocimetry reveals multiphase flow field perturbations in porous media. *Proceedings of the National Academy of Sciences*, 121(12): e2316723121, 2024. doi: [10.1073/pnas.2316723121](https://doi.org/10.1073/pnas.2316723121). URL <https://www.pnas.org/doi/abs/10.1073/pnas.2316723121>.
- [31] Tom Brown, Benjamin Mann, Nick Ryder, Melanie Subbiah, Jared D Kaplan, Prafulla Dhariwal, Arvind Neelakantan, Pranav Shyam, Girish Sastry, Amanda Askell, et al. Language models are few-shot learners.

- Advances in neural information processing systems, 33:1877–1901, 2020.
- [32] Kaiming He, Xiangyu Zhang, Shaoqing Ren, and Jian Sun. Deep residual learning for image recognition. In Proceedings of the IEEE conference on computer vision and pattern recognition, pages 770–778, 2016.
- [33] John Jumper, Richard Evans, Alexander Pritzel, Tim Green, Michael Figurnov, Olaf Ronneberger, Kathryn Tunyasuvunakool, Russ Bates, Augustin Žídek, Anna Potapenko, et al. Highly accurate protein structure prediction with AlphaFold. nature, 596(7873):583–589, 2021.
- [34] Mohammed Yaqoob, Mohammed Yusuf Ansari, Mohammed Ishaq, Unais Ashraf, Saideep Pavuluri, Arash Rabbani, Harris Sajjad Rabbani, and Thomas D. Seers. Fluidnet-lite: Lightweight convolutional neural network for pore-scale modeling of multiphase flow in heterogeneous porous media. Advances in Water Resources, 200:104952, 2025. ISSN 0309-1708. doi: <https://doi.org/10.1016/j.advwatres.2025.104952>. URL <https://www.sciencedirect.com/science/article/pii/S0309170825000661>.
- [35] Alvaro Sanchez-Gonzalez, Jonathan Godwin, Tobias Pfaff, Rex Ying, Jure Leskovec, and Peter W. Battaglia. Learning to simulate complex physics with graph networks. In Proceedings of the 37th International Conference on Machine Learning, ICML’20. JMLR.org, 2020.
- [36] Gege Wen, Zongyi Li, Qirui Long, Kamyar Azizzadeneheli, Anima Anandkumar, and Sally M Benson. Real-time high-resolution co₂ geological storage prediction using nested fourier neural operators. Energy & Environmental Science, 16(4):1732–1741, 2023.
- [37] Cristian Bodnar, Wessel P Bruinsma, Ana Lucic, Megan Stanley, Anna Allen, Johannes Brandstetter, Patrick Garvan, Maik Riechert, Jonathan A Weyn, Haiyu Dong, et al. A foundation model for the earth system. Nature, pages 1–8, 2025.
- [38] Zongyi Li, Daniel Zhengyu Huang, Burigede Liu, and Anima Anandkumar. Fourier neural operator with learned deformations for pdes on general geometries. Journal of Machine Learning Research, 24(388):1–26, 2023.
- [39] Guang Yang, Ran Xu, Yusong Tian, Songyuan Guo, Jingyi Wu, and Xu Chu. Data-driven methods for flow and transport in porous media: A review. International Journal of Heat and Mass Transfer, 235:126149, 2024.
- [40] Dominik Müller, Iñaki Soto-Rey, and Frank Kramer. Towards a guideline for evaluation metrics in medical image segmentation. BMC Research Notes, 15:210, 2022. doi: 10.1186/s13104-022-06096-y.
- [41] Omid Tavakkoli, Ying Da Wang, Peyman Mostaghimi, and Ryan T. Armstrong. A pore morphology-based initializer to accelerate lattice boltzmann simulations of capillary-dominated flow with variable wettability. Physics of Fluids, 37(9):092125, Sept 2025. ISSN 1070-6631. doi: 10.1063/5.0285656. URL <https://doi.org/10.1063/5.0285656>.
- [42] James E. McClure, Zhe Li, Mark Berrill, and Thomas Ramstad. The lbpm software package for simulating multiphase flow on digital images of porous rocks. Computational Geosciences, 25(3):871–895, June 2021. ISSN 1420-0597. doi: 10.1007/s10596-020-10028-9. Publisher Copyright: © 2021, The Author(s), under exclusive licence to Springer Nature Switzerland AG part of Springer Nature.
- [43] Berken Agaoglu, Nadim K. Coptly, Traugott Scheytt, and Reinhard Hinkelmann. Interphase mass transfer between fluids in subsurface formations: A review. Advances in Water Resources, 79:162–194, May 2015. ISSN 0309-1708. doi: 10.1016/j.advwatres.2015.02.009. URL <https://www.sciencedirect.com/science/article/pii/S0309170815000354>.
- [44] Chaoqun Yao, Yuchao Zhao, Haiyun Ma, Yanyan Liu, Qiankun Zhao, and Guangwen Chen. Two-phase flow and mass transfer in microchannels: A review from local mechanism to global models. Chemical Engineering Science, 229:116017, 2021. ISSN 0009-2509. doi: <https://doi.org/10.1016/j.ces.2020.116017>. URL <https://www.sciencedirect.com/science/article/pii/S0009250920305492>.
- [45] Ryan T. Armstrong, James E. McClure, Vanessa Robins, Zhishang Liu, Christoph H. Arns, Steffen Schlüter, and Steffen Berg. Porous media characterization using minkowski functionals: Theories, applications and future directions. Transport in Porous Media, 130(1):305–335, October 2019. ISSN 1573-1634. doi: 10.1007/s11242-018-1201-4. URL <https://doi.org/10.1007/s11242-018-1201-4>.
- [46] Qingqi Zhao, Xiaoxue Han, Ruichang Guo, and Cheng Chen. A computationally efficient hybrid neural network architecture for porous media: Integrating convolutional and graph neural networks for improved property predictions. Advances in Water Resources, 195:104881, 2025.
- [47] D. Lee, F. Weinhardt, J. Hommel, J. Piotrowski, H. Class, and H. Steeb. Machine learning assists in increasing the time resolution of x-ray computed tomography applied to mineral precipitation in porous media. Scientific Reports, 13(1):10529, 2023. doi: 10.1038/s41598-023-37523-0.

- [48] Daniel B. Allan, Thomas Caswell, Nathan C. Keim, Casper M. van der Wel, and Ruben W. Verweij. `soft-matter/trackpy`: Trackpy v0.5.0, April 2021. URL <https://doi.org/10.5281/zenodo.4682814>.
- [49] Olaf Ronneberger, Philipp Fischer, and Thomas Brox. U-net: Convolutional networks for biomedical image segmentation. In Nassir Navab, Joachim Hornegger, William M. Wells, and Alejandro F. Frangi, editors, Medical Image Computing and Computer-Assisted Intervention – MICCAI 2015, page 234–241, Cham, 2015. Springer International Publishing. ISBN 978-3-319-24574-4. doi: 10.1007/978-3-319-24574-4_28.
- [50] Songyou Peng, Michael Niemeyer, Lars Mescheder, Marc Pollefeys, and Andreas Geiger. Convolutional occupancy networks. In European Conference on Computer Vision, pages 523–540. Springer, 2020.
- [51] J Ryan Shue, Eric Ryan Chan, Ryan Po, Zachary Ankner, Jiajun Wu, and Gordon Wetzstein. 3D Neural Field Generation using Triplane Diffusion. In Proceedings of the IEEE/CVF Conference on Computer Vision and Pattern Recognition, pages 20875–20886, 2023.
- [52] Biao Zhang, Jiapeng Tang, Matthias Niessner, and Peter Wonka. 3DShape2VecSet: A 3D Shape Representation for Neural Fields and Generative Diffusion Models. ACM Transactions On Graphics (TOG), 42(4):1–16, 2023.

Appendix

Learning Pore-scale Multiphase Flow from 4D Velocimetry

S1 Training Details and Model Parameters

The particle-scale velocity prediction component of our framework is based on a Graph Neural Network (GNS) architecture trained using an autoregressive rollout strategy. Node features consist of two-step particle positions (6 features) and a velocity history over $C = 5$ steps (15 features), resulting in a total of 21 input features per node. Edge attributes include two-step pairwise relative positions (6 features) and their ℓ_2 norm (1 feature), yielding 7 edge features per edge. A graph is constructed at each time step using a radius-based criterion with $r = 32$ voxels and a maximum of 64 neighbors per node.

The GNS employs 10 message-passing layers, each comprising residual connections and fully connected update functions with 128 hidden dimensions. A CNN-based encoder integrates local geometry information extracted from voxel patches centered on each particle, downsampled from the original CT data. The final decoder predicts three-dimensional particle velocities at the next time step.

Data normalization is applied based on statistics computed from the entire training set. Models are optimized with Adam optimizer, with a learning rate of 5×10^{-5} , weight decay of 5×10^{-4} , and a cosine annealing learning rate schedule with $T_{\max} = 200$ epochs. Models are trained for 600 epochs with a batch size of 1, on a single NVIDIA A100 (80GB) GPU.

To improve rollout robustness, we adopt a noise injection strategy similar to that used in the original GNS framework. Specifically, during training, Gaussian noise is added to the ground truth particle positions used to construct the input graph, encouraging the model to learn stable dynamics under small perturbations. This helps mitigate compounding errors during autoregressive inference.

The interface morphology component uses a 3D U-Net trained to predict binary fluid occupancy at the next time step, conditioned on a history of $N_{\text{in}} = 2$ previous segmented interface fields, corresponding velocity fields, and the static pore geometry. Input channels include three velocity components, one binary interface channel per frame, and an optional pore geometry mask. The network employs a standard encoder-decoder structure with skip connections, trained using binary cross-entropy loss.

U-Net is trained for 100 epochs with a batch size of 2, using the Adam optimizer with a learning rate of 10^{-3} . Mixed-precision training with automatic casting to FP16 is enabled to improve computational efficiency. Data downsampling by a factor of 8 is applied to both velocity and geometry fields for memory efficiency. The dataset is divided temporally, with 75% used for training and 25% reserved for testing.

S2 Failure Mode Analysis

Fig. S1 illustrates two representative failure modes of the learned framework under extended autoregressive rollout and cross-rock domain shift. During long-horizon prediction (Fig. S1A), the model maintains strong agreement with the ground truth at early timesteps (frames 15–45), but small velocity and interface discrepancies accumulate over time, leading to visible deviations by frame 70. This temporal degradation is reflected in the gradual increase in RMSE and decrease in R^2 toward the end of the rollout.

Under strict zero-shot inference on the Ketton limestone sample (Fig. S1B), the global velocity statistics remain well correlated with experimental measurements; however, localized regions exhibit reduced trajectory alignment and flow direction consistency. These failure modes highlight the sensitivity of autoregressive dynamics to compounding errors and the challenges posed by pronounced pore-structure domain shifts.

S3 Supplementary Training Data

To improve in-domain generalization and assess robustness to experimental variability, we augment the training set with two additional drainage experiments acquired from the same sintered-glass sample used in Exp. α . These experiments,

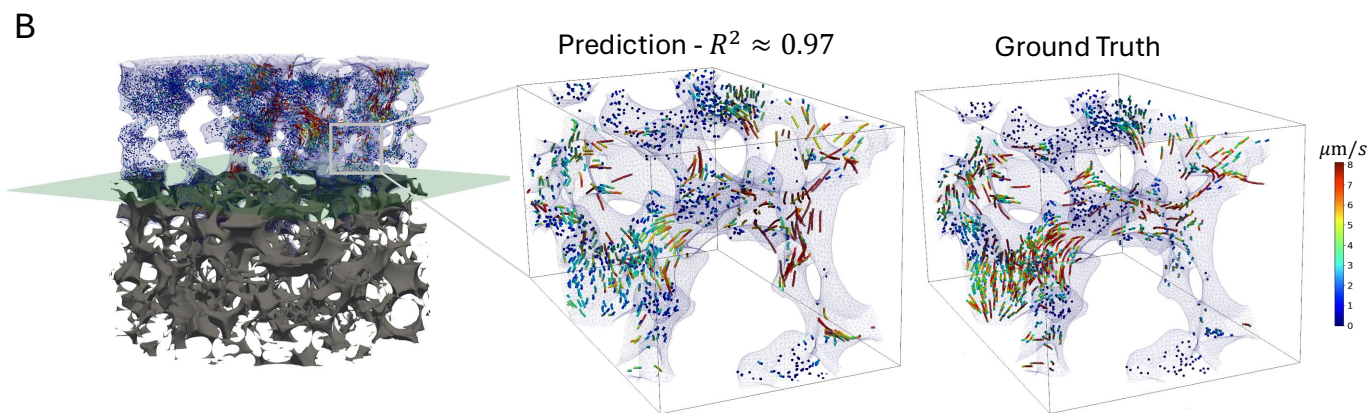
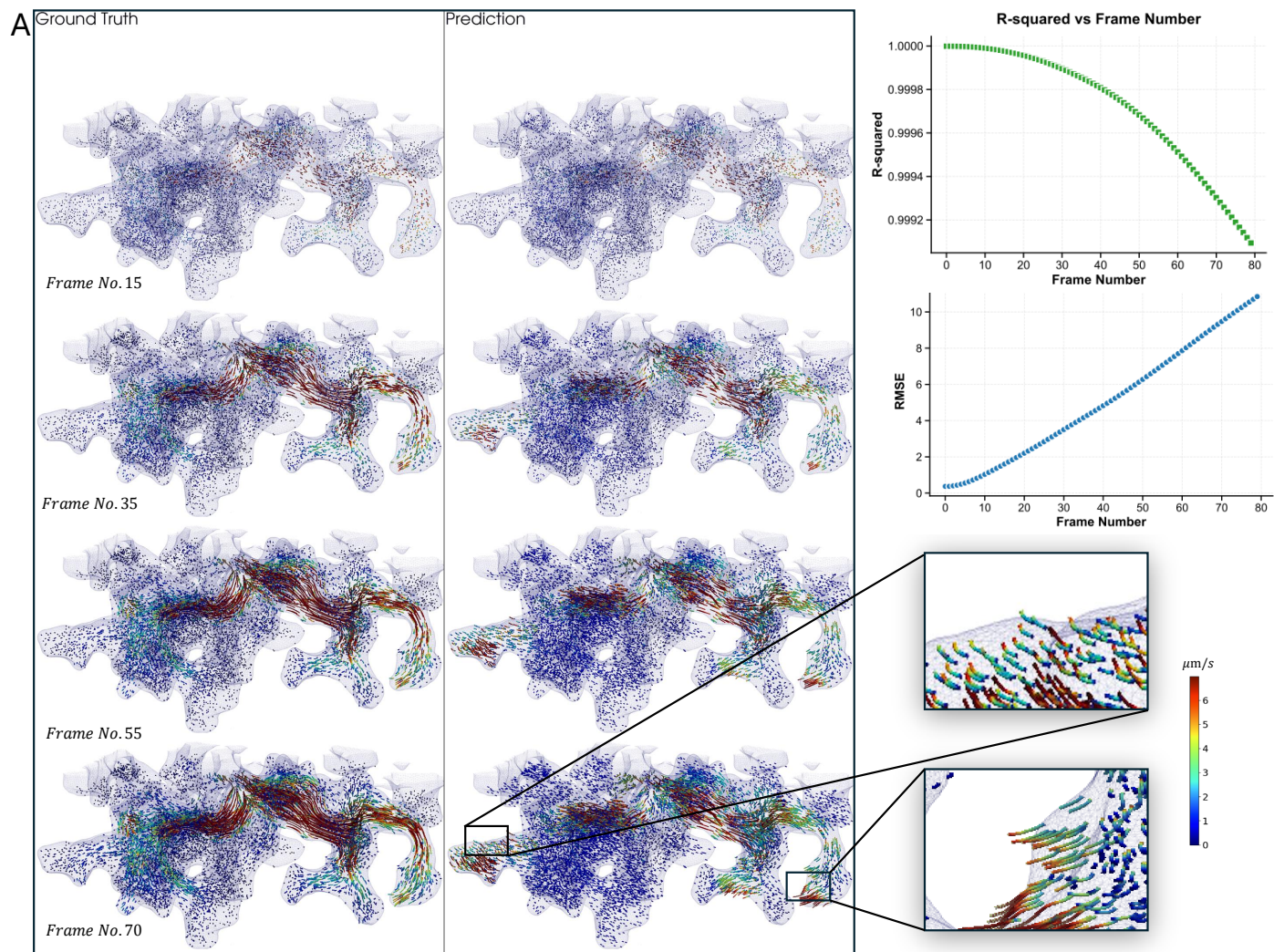


Figure S1 Failure modes of the learned rollout under long-horizon prediction and cross-rock generalization. (A) Extended rollout failure. Predicted interface evolution and particle velocities remain consistent with the ground truth at early timesteps (frames 15–45), but visible deviations emerge by frame 70 as errors accumulate autoregressively. This degradation is reflected in the increasing RMSE and decreasing R^2 over time, particularly toward the end of the rollout. **(B)** Generalization-induced failure under cross-rock shift. Zero-shot inference on a Ketton limestone sample using a model trained exclusively on sintered-glass data. While the overall velocity field and particle statistics remain well correlated with the ground truth, localized regions exhibit degraded trajectory tracking and velocity alignment, highlighting limitations under pronounced pore-structure domain shift.

denoted Exp. α' and Exp. α'' , are performed on the identical porous medium, ensuring that all three datasets share the same pore geometry.

Both supplementary experiments are conducted at an injection rate of 348 nL/min. Exp. α' is acquired at a temporal resolution of 0.5 s per frame, yielding 100 frames. To maintain consistency with the main dataset, the sequence is temporally interpolated to a resolution of 0.25 s per frame. Exp. α'' is recorded directly at 0.25 s per frame with 100 frames captured.

The model is trained jointly on Exp. α , Exp. α' , and Exp. α'' . For each dataset, the final 25% of frames in time are held out and used as test data, while the remaining frames are used for training. Performance on the held-out portions of Exp. α' and Exp. α'' is reported in Fig. S2, including trajectory-based R^2 metrics and comparisons of velocity-component distributions.

The model trained on the combined sintered-glass dataset is subsequently used, without any fine-tuning, to perform strict zero-shot inference on the Ketton limestone experiment described in the main text.

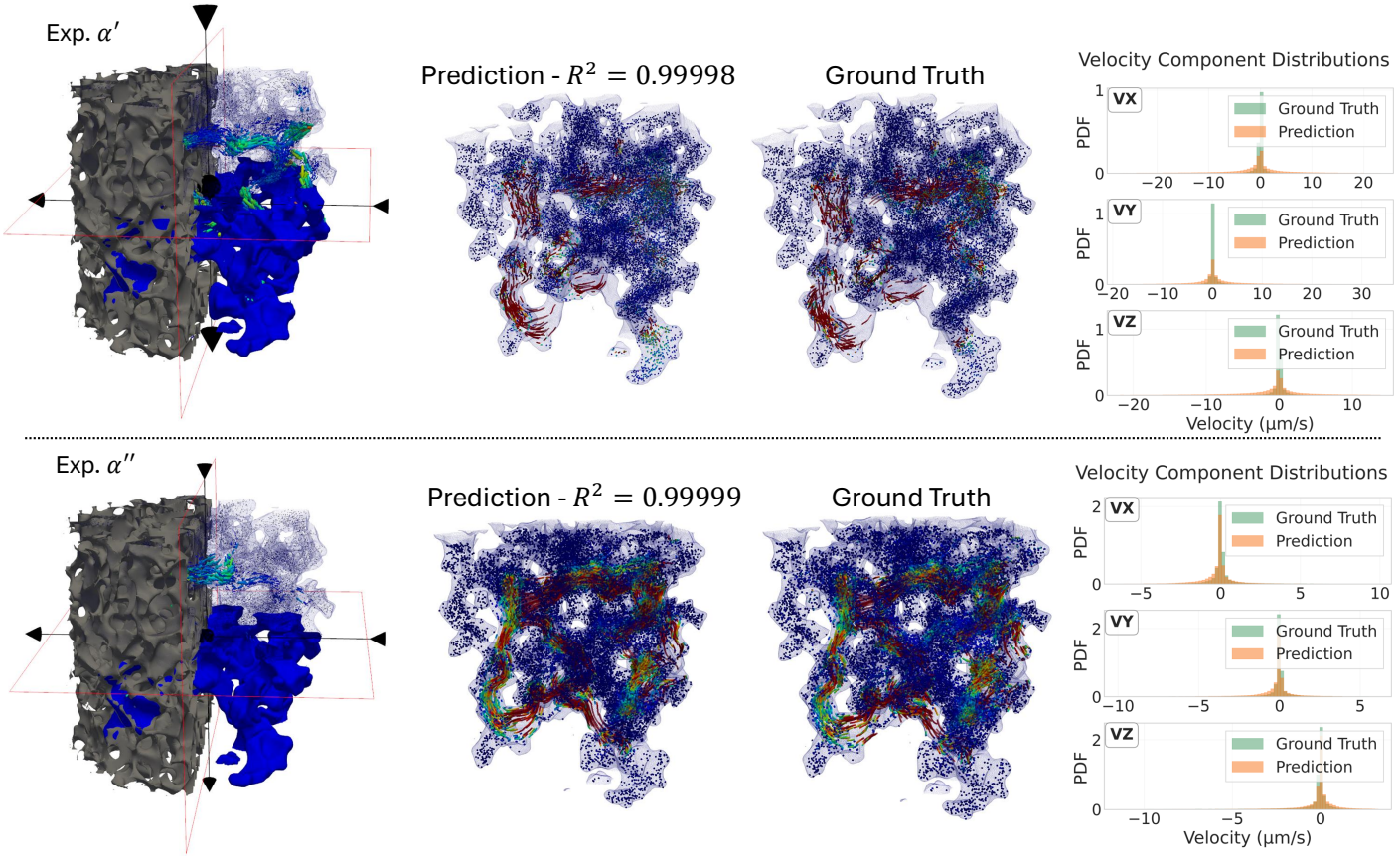


Figure S2 Supplementary training data for improved in-domain generalization. Two additional drainage experiments from the sintered-glass sample used in Exp. α (Exp. α' and Exp. α'') are incorporated into training. The data are split into two folds, with performance evaluated on the corresponding held-out test sets. Reported metrics include R^2 computed from tracer trajectory agreement and comparisons of velocity-component distributions between predictions and ground truth for both experiments.

S4 Max-Pooling for Velocity Field Downsampling

Efficient downsampling of particle velocity data is essential for integrating Lagrangian particle information into grid-based learning frameworks while controlling memory usage. In our workflow, particle velocities are first interpolated onto a regular voxel grid that spans the pore space. To further reduce resolution without excessive information loss, we apply a custom three-dimensional pooling operation.

The pooling is performed over cubic blocks of size $f \times f \times f$, where f is the downsampling factor. For each block, the

output value is determined by selecting the element (maximum or minimum) with the larger absolute value:

$$\mathcal{P}_{ijk} = \begin{cases} \max(\mathcal{B}_{ijk}) & \text{if } |\max(\mathcal{B}_{ijk})| \geq |\min(\mathcal{B}_{ijk})|, \\ \min(\mathcal{B}_{ijk}) & \text{otherwise.} \end{cases}$$

Here, \mathcal{B}_{ijk} represents the set of velocity values within the (i, j, k) -th pooling block, and \mathcal{P}_{ijk} is the pooled result. This approach ensures that dominant features with high magnitude, such as regions of strong flow, sharp gradients, or boundary layer structures, are preferentially retained during the downsampling process.

Naïve downsampling techniques, such as uniform subsampling or simple averaging, are known to cause severe information loss in three-dimensional datasets, particularly when representing sparse or high-contrast physical fields as in particle velocity. Such methods often fail to preserve critical flow features, resulting in degraded model inputs and reduced prediction accuracy. The pooling operation adopted here mitigates this problem by selectively preserving velocity extremes within each spatial block, maintaining essential flow information while reducing data dimensionality.

In practice, we apply this pooling operation with a downsampling factor of $f = 8$, which provides a favorable balance between memory efficiency and preservation of key velocity structures critical for learning accurate flow-interface interactions.

S5 Flow Field Reconstruction Details

To evaluate model-predicted Lagrangian particle velocities against voxel-based experimental flow fields, we reconstruct a dense Eulerian velocity field via interpolation. Given a set of predicted particle velocities $\{\mathbf{v}_i\}$ at spatial positions $\{\mathbf{x}_i\}$ within the pore space, we interpolate onto a uniform voxel grid using a physically constrained method.

For each velocity component, we augment the interpolation set with boundary points sampled from the fluid–solid interface, identified by morphological dilation of the solid-phase mask. These boundary points $\{\mathbf{x}_b\}$ are assigned zero velocity to enforce the no-slip condition. The interpolation problem then becomes:

$$\mathbf{v}(\mathbf{x}) = \text{Interp}(\{\mathbf{x}_i, \mathbf{x}_b\}, \{\mathbf{v}_i, \mathbf{0}\}; \mathbf{x}),$$

where Interp denotes trilinear interpolation over the combined particle and boundary constraints.

A tunable ratio ρ controls the number of boundary points relative to velocity-carrying particles, balancing computational efficiency and fidelity near walls. The resulting velocity field is masked by the pore geometry to remove any spurious values in the solid domain. This procedure yields a continuous voxel-based velocity field suitable for direct comparison with experimental measurements using standard metrics such as MAE and spatial correlation.

S6 SDF-Based Interpolation of Fluid Interfaces Between Temporal Frames

To bridge the temporal resolution mismatch between training (0.25 s) and test data (0.5 s), we interpolate intermediate fluid interfaces between observed frames. This allows autoregressive rollout at the model’s native time scale using temporally consistent inputs.

Given binary pore segmentation V_0 and V_1 at consecutive time steps, we compute their corresponding signed distance fields (SDFs), defined as

$$\phi_i(\mathbf{x}) = d_{\text{in}}^i(\mathbf{x}) - d_{\text{out}}^i(\mathbf{x}), \quad i \in \{0, 1\},$$

where d_{in}^i and d_{out}^i are Euclidean distance transforms of the foreground and background regions, respectively. Intermediate geometries are obtained by linear interpolation in SDF space:

$$\phi_t(\mathbf{x}) = (1 - t)\phi_0(\mathbf{x}) + t\phi_1(\mathbf{x}), \quad t \in [0, 1],$$

followed by thresholding $\phi_t(\mathbf{x}) \geq 0$ to produce a binary mask. This method ensures smooth geometric transitions between frames and preserves physical continuity in interface evolution.

S7 Trajectory Smoothing Using a Constant-Acceleration Kalman Smoother

Raw particle trajectories obtained from micro-velocimetry contain localization noise due to imaging artifacts, sub-voxel interpolation, and tracking uncertainty. Differentiating such noisy positions to obtain velocities amplifies high-frequency errors, producing non-physical velocity spikes and jitter that can dominate the learning signal in data-driven models.

To obtain smoother trajectories while preserving transient dynamics, we employ a model-based state-space approach: a 3D constant-acceleration (CA) Kalman filter followed by Rauch–Tung–Striebel (RTS) backward smoothing. The CA model treats each particle as evolving according to

$$\mathbf{s}_t = [x_t, \dot{x}_t, \ddot{x}_t, y_t, \dot{y}_t, \ddot{y}_t, z_t, \dot{z}_t, \ddot{z}_t]^\top \in \mathbb{R}^9,$$

with a discrete-time transition

$$\mathbf{s}_{t+1} = \mathbf{F}(\Delta t) \mathbf{s}_t + \mathbf{w}_t,$$

where $\mathbf{F}(\Delta t)$ is the standard CA kinematic matrix (position integrates velocity and acceleration, and velocity integrates acceleration), and $\mathbf{w}_t \sim \mathcal{N}(\mathbf{0}, \mathbf{Q})$ represents process noise. In our implementation, \mathbf{Q} is derived from a white-jerk assumption (acceleration driven by random jerk), which permits smooth but flexible changes in acceleration between frames.

The measurement model uses only observed positions,

$$\mathbf{z}_t = \mathbf{H} \mathbf{s}_t + \mathbf{v}_t, \quad \mathbf{H} \mathbf{s}_t = [x_t, y_t, z_t]^\top,$$

with $\mathbf{v}_t \sim \mathcal{N}(\mathbf{0}, \mathbf{R})$ representing measurement noise. The forward Kalman recursion produces filtered state estimates and covariances that optimally fuse the motion prior with noisy observations under Gaussian assumptions. RTS smoothing then performs a backward pass to compute a globally consistent trajectory estimate that leverages information from both past and future frames, substantially reducing lag and edge artifacts relative to causal filters.

This Kalman smoother is well matched to our application because it (i) enforces a physically interpretable kinematic prior (continuous velocity and acceleration); and (ii) directly outputs denoised positions and velocities in a single procedure.

S8 Velocity Prediction Error Metric

We report velocity prediction accuracy using $\text{NRMSE}_{\text{p99}}$, defined below, to provide a stable reference scale for comparison across datasets. Standard per-particle mean relative error (MRE) can be sensitive to capillary-dominated drainage experiments, where a substantial fraction of tracer particles are effectively stagnant between drainage events. In the Ketton limestone dataset, for example, 43.9% of particle-frame observations have a ground-truth velocity magnitude below 0.1 vox/frame, and the corresponding fraction is 48.2% for the in-distribution sintered-glass dataset (Exp. α). Both velocity distributions are strongly right-skewed: mean-to-median ratios are 4.7 for the sintered-glass dataset and 1.9 for Ketton, confirming that the typical particle is effectively stagnant even as a small fraction of fast-moving particles drives the drainage dynamics. Velocities at or below 0.1 vox/frame fall within the experimental precision, so relative-error calculations in this regime can be dominated by measurement noise and are not preferred for error assessment. For such particles, the denominator of the relative error,

$$\epsilon_{\text{rel},i} = \frac{|\|\hat{\mathbf{v}}_i\| - \|\mathbf{v}_{\text{gt},i}\||}{\|\mathbf{v}_{\text{gt},i}\|},$$

approaches zero, which can produce large $\epsilon_{\text{rel},i}$ values even when the absolute prediction error is sub-voxel. These near-stagnant particles are less informative for the model’s capacity to predict advective transport: their positional uncertainty is dominated by sub-voxel localisation noise and tracking artefacts rather than by dynamically meaningful flow. Accordingly, we prioritize metrics that reflect advective transport rather than measurement noise in near-stagnant regions.

To obtain a physically meaningful and numerically stable accuracy measure, we adopt the normalised root-mean-square

error relative to the 99th-percentile characteristic velocity (NRMSE_{p99}), defined as

$$\text{NRMSE}_{p99} = \frac{\text{RMSE}(\|\mathbf{v}\|)}{Q_{99}(\|\mathbf{v}_{\text{gt}}\|)}, \quad \text{RMSE}(\|\mathbf{v}\|) = \sqrt{\frac{1}{N} \sum_{i=1}^N (\|\hat{\mathbf{v}}_i\| - \|\mathbf{v}_{\text{gt},i}\|)^2}, \quad (\text{S1})$$

where $\hat{\mathbf{v}}_i$ and $\mathbf{v}_{\text{gt},i}$ are the predicted and ground-truth velocity vectors for particle i , N is the total number of particles, and $Q_{99}(\|\mathbf{v}_{\text{gt}}\|)$ denotes the 99th percentile of the ground-truth velocity-magnitude distribution computed over all particles and frames. This metric has three desirable properties.

1. **All particles are included.** Unlike threshold-based filters, which discard slow-moving particles and introduce selection bias, NRMSE_{p99} uses the full particle set. Near-stagnant particles contribute a small absolute error to the RMSE numerator proportional to their actual prediction error, rather than inflating a relative denominator.
2. **Physically motivated reference scale.** The 99th-percentile velocity Q_{99} is a reasonable estimate of the characteristic fast-particle velocity—the upper end of the advective flow regime—without being dominated by isolated outliers. Normalising by this quantity expresses the prediction error as a fraction of the characteristic flow speed, analogous to normalising by the free-stream velocity U_∞ in external-flow computational fluid dynamics validation.
3. **Robustness to distributional skewness.** Velocity magnitudes in porous-media flow are highly right-skewed: a few fast particles in preferential flow paths coexist with a majority of slow or stagnant particles. The 99th percentile captures the scale of the fast-flow regime without being inflated by extreme outliers (as the maximum would be) or suppressed by the stagnant majority (as the mean would be).

For the Ketton limestone zero-shot dataset (frames 150–180, $N = 380\,370$ particles), the ground-truth 99th-percentile velocity magnitude is $Q_{99} = 1.315$ vox/frame, and the RMSE is 0.2150 vox/frame, yielding $\text{NRMSE}_{p99} = 16.4\%$. For reference, the in-distribution sintered-glass dataset (Exp. α) has a 99th-percentile velocity of $Q_{99} = 4.700$ vox/frame, reflecting the substantially higher characteristic flow speeds in that experiment.